Four-wave mixing instabilities in photonic-crystal and tapered fibers

F. Biancalana, D. V. Skryabin, and P. St. J. Russell
Department of Physics, University of Bath, Bath BA2 7AY, United Kingdom
(Received 9 May 2003; published 13 October 2003)

Four-wave mixing instabilities are theoretically studied for continuous wave propagation in ultrasmall core photonic-crystal and tapered fibers. The waveguide, or geometrical, contribution to the overall dispersion of these structures is much stronger than in conventional fibers. This leads to the appearance of unstable frequency bands that are qualitatively and quantitatively different from those seen in conventional fibers. The four-wave mixing theory developed here is based on the full wave equation, which allows rigorous study of the unstable bands even when the detunings are of the order of the pump frequency itself. Solutions obtained using the generalized nonlinear Schrödinger equation, which is an approximate version of the full wave equation, reveal that it suffers from several deficiencies when used to describe four-wave mixing processes.

DOI: 10.1103/PhysRevE.68.046603 PACS number(s): 42.81.−i

I. INTRODUCTION

Four-wave mixing (FWM) is a fundamental nonlinear optical process, in which a pair of Stokes and anti-Stokes photons is generated from two pump photons through the third-order nonlinear susceptibility. FWM can be observed in a wide range of materials, including optical fibers [1]. The existence and efficiency of frequency conversion by FWM crucially depend on the so-called phase-matching conditions [1], which are in turn determined by the dispersive properties of the system. Modulational instability (MI) of continuous wave (CW) radiation is a kind of FWM instability and is well known in conventional optical fibers, where the dispersion profile is well approximated by a group velocity dispersion (GVD) that is either independent of, or linearly dependent on, frequency [1].

Recent advances in the fabrication of photonic-crystal fibers (PCFs) [2–5] have made possible the production of fibers with tiny core areas and dispersion characteristics that are strongly modified compared to conventional fibres. As a consequence, the FWM phase-matching conditions are completely different from those seen in conventional fibers. An additional advantage of small-core PCFs is that strong nonlinear interactions occur at relatively low peak powers and over short propagation distances. For these reasons, PCFs offer the opportunity to develop a new family of parametric amplifiers and oscillators.

The dispersion characteristics of tapered fibers (TFs), see, e.g., Ref. [6], which are made by heating and stretching conventional fibers, are very similar to those in small-core PCFs. A typical TF is a transversely homogeneous strand of silica glass with diameter around 1 or 2 μm. The GVD profiles of PCFs and TFs are similar because, in a typical index-guiding PCF, most of the light is guided in a tiny silica core surrounded by a periodic structure of large air-filled holes separated by thin silica membranes, a structure that has strong similarities to a TF. A disadvantage of TFs compared to PCFs is that they are fragile and, therefore, are practical only in short lengths (<1 m).

Several recent papers on FWM in PCFs [7–10] have focused their theories on cases when FWM instabilities excite bands of gain analogous to the MI bands seen in conventional fibers [1]. The results in these papers can essentially be described within the framework of the idealized nonlinear Schrödinger (NLS) equation, which means that they do not contain any new features specific to the ultrasmall core fibers studied here. The main aim of this work is to reveal these features. In order to achieve this in a rigorous manner we develop a theory of FWM which goes beyond the slowly varying envelope approximation of the NLS equation and deals directly with the wave equation. Our analysis reveals the existence of different instability bands and shows the possibility of backward wave excitation. A detailed comparison with the results obtained using a generalized version of the nonlinear Schrödinger equation reveals several deficiencies of the latter.

II. FWM INSTABILITIES BEYOND SLOWLY VARYING APPROXIMATION

We start our analysis with the nonlinear wave equation derived directly from Maxwell's equations:

$$\vec{\nabla}^2\vec{E}-\vec{\nabla}(\vec{\nabla}\cdot\vec{E})-\frac{1}{c^2}\partial_t^2(\vec{E}-\vec{P}_L-\vec{P}_{NL})=\vec{0}, \tag{1}$$

where $\vec{\nabla}=\vec{i}\,\partial_x+\vec{j}\,\partial_y+\vec{k}\,\partial_z$. The linear polarization is defined as

$$\vec{P}_L=\int_{-\infty}^{\infty}\chi^{(1)}(t-t',x,y)\vec{E}(t')dt', \tag{2}$$

where $\vec{E}$ is the electric field, and $\chi^{(1)}$ is the linear susceptibility of the dielectric medium (in our case silica glass), which depends on time and the transverse coordinates x,y. $\vec{P}_{NL}$ includes both Kerr and Raman terms:

$$\vec{P}_{NL}=\frac{3}{4}\chi_3\left[(1-\theta)|\vec{E}|^2+\theta\int_{-\infty}^{+\infty}g(t-t')|\vec{E}(t')|^2dt'\right]\vec{E}, \tag{3}$$

where $\theta\simeq 0.18$ measures the relative strength of the instantaneous and noninstantaneous nonlinearities [1] and

$$g(t)=\frac{\tau_1^2+\tau_2^2}{\tau_1\tau_2^2}e^{-t/\tau_2}\sin(t/\tau_1)\Theta(t). \tag{4}$$

Here $\tau_1\simeq 12.2$ fs is the inverse of the phonon frequency taken relative to the pump frequency and $\tau_2\simeq 32$ fs is the phonon lifetime [1]. $\Theta(t)$ is the Heaviside function and $\chi_3\simeq 10^{-19}$ m^2/W is the nonlinear susceptibility.

Our next step is to reduce Eq. (1) to an equation in z and t only. In order to achieve this we first transform Eq. (1) from the time to the frequency domain, using Fourier transform $\mathcal{F}$, and then separate transverse and longitudinal degrees of freedom through the approximate factorization $\mathcal{F}\vec{E}(x,y,z,t)=\hat{\vec{E}}(x,y,z,\omega)\simeq\vec{F}(x,y,\omega)\tilde{E}(z,\omega)$. $\vec{F}$ is an eigenmode of the linear waveguide having propagation constant $k(\omega)$ where ω is the optical frequency. $k(\omega)$ incorporates both material and waveguide contributions to the overall fiber dispersion, and it is calculated by solving the eigenvalue problem for the time- and z-independent cases (see, e.g., Ref. [11]).

It can be shown that the dynamics of the inverse Fourier transform $\mathcal{F}^{-1}\tilde{E}=\overline{E}(z,t)$ of the amplitude $\tilde{E}$ are governed by the equation

$$\begin{aligned}c^2\partial_z^2\overline{E}-\partial_t^2\overline{E}=\partial_t^2\Bigg[&\int_{-\infty}^{+\infty}\chi_{eff}^{(1)}(t-t')\overline{E}(t')dt'\\&+(1-\theta)\overline{\chi}^{(3)}|\overline{E}|^2\overline{E}+\theta\overline{\chi}^{(3)}\overline{E}(t)\\&\times\int_{-\infty}^{+\infty}g(t-t')|\overline{E}(t')|^2dt'\Bigg],\end{aligned} \tag{5}$$

where $\chi_{eff}^{(1)}$ is the effective linear susceptibility of the fibre, with its Fourier transform, $\mathcal{F}\chi_{eff}^{(1)}=\hat{\chi}_{eff}^{(1)}(\omega)$, being given by

$$\hat{\chi}_{eff}^{(1)}(\omega)=\frac{k^2c^2}{\omega^2}-1 \tag{6}$$

and $\overline{\chi}_3=3S_{mod}\chi_3/(4S_{eff})$. Here $S_{mod}=\int|\vec{F}|^2dS$ is the modal area and $S_{eff}=S_{mod}^2/(\int|\vec{F}|^4dS)$. In what follows we make the approximation that $S_{mod}\simeq S_{eff}\simeq\pi d^2/4$, where d is the core diameter. We also assume that $\hat{\chi}_{eff}^{(1)}(\omega)$ is real, i.e., we disregard any linear loss. For the sake of brevity, from now on we will write $\hat{\chi}(\omega)$ instead of $\hat{\chi}_{eff}^{(1)}(\omega)$.

The calculated frequency dependence of the GVD, $\beta_2=\partial_\omega^2k(\omega)$, for a TF with $d=1$ μm is plotted in Fig. 1 together with the experimentally measured dispersion profile of a PCF with a 1.2-μm core surrounded by air holes of approximately the same size (but separated by glass membranes 0.13 μm thick). In conventional telecom fibers the diameter of the guiding core is $\simeq 9$ μm. Thus the ratio of core diameter to wavelength in the fibers considered here is much less than in conventional ones. For this reason these fibers can be termed as both strongly guiding and highly nonlinear.

The GVD profiles for TF and PCF shown in Fig. 1 are very similar. There are two zero GVD points with a region of anomalous dispersion in between them. $\beta_3=\partial_\omega^3k(\omega)$ is positive at the right hand, i.e., high-frequency, zero GVD point. An analog of this zero dispersion point, where $\beta_2=0$ and $\beta_3>0$, is well known in conventional fibers, where it occurs at $\omega/(2\pi)\simeq 229$ THz (see Fig. 1 for an example of the GVD profile of Corning SMF28 fiber). In our fibers this point is shifted far towards the blue side of the spectrum. A second zero dispersion point occurs close to $\omega/(2\pi)\simeq 235$ THz, where in addition $\beta_3<0$. Thus the entire range of anomalous dispersion is shifted significantly towards the blue side of the spectrum. Increasing the core diameter causes the zero GVD points to shift towards smaller frequencies, when the dispersion profiles become similar to those seen in conventional fibers. Note that the coexistence of two zero GVD points within an experimentally relevant frequency range has a profound effect on the FWM instabilities discussed below.

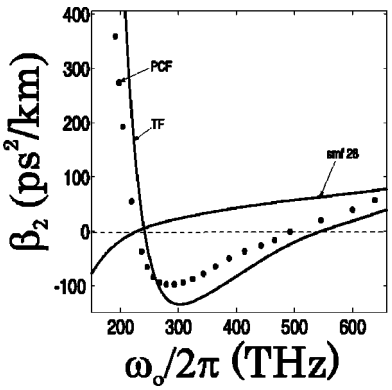

FIG. 1. GVD parameters as functions of frequency: for the 1.2-μm-core PCF (Optoelectronics group, Bath), for the 1-μm tapered fiber (TF), and conventional fiber (Corning SMF28).

We now assume that the fiber is pumped by a CW signal

$$\overline{E}=\frac{1}{\sqrt{S_{mod}}}E_0e^{i(z\sqrt{k_0^2+K_0^2}-\omega_0t)}+\text{c.c.}, \tag{7}$$

where E_0 is a constant amplitude, $\sqrt{k_0^2+K_0^2}$ and ω_0 are, respectively, the wave vector and the frequency of the pump wave. $k_0=k(\omega_0)$ characterizes the linear, i.e., power independent, part of the wave vector, while K_0 is intensity dependent. Expression (7) is a solution to Eq. (5) provided that

$$K_0^2=2k_0\gamma|E_0|^2,\quad \gamma=(\omega_0^2\overline{\chi}^{(3)})/(2k_0c^2S_{mod}), \tag{8}$$

where γ is the standard parameter used to characterize the nonlinear properties of fibers [1].

To explore the FWM gain, we perturb solution (7) with a small complex signal ϵ:

$$\overline{E}=\frac{1}{\sqrt{S_{mod}}}[E_0+\epsilon(z,t)]e^{i(z\sqrt{k_0^2+K_0^2}-\omega_0t)}+\text{c.c.} \tag{9}$$

After substituting Eq. (9) into the governing equation (5) we disregard all the terms nonlinear in ϵ. We then take ϵ in the general and convenient form of a superposition of Stokes and anti-Stokes waves:

$$\epsilon(z,t)=\int d\delta \sum_j \left[u_j^{AS}e^{i\kappa_j z-i\delta t}+u_j^{S}e^{-i\kappa_j^{*}z+i\delta t}\right] \quad (10)$$

and derive a linear equation for the vectors $\vec{\xi}_j=(u_j^{AS},(u_j^{S})^{*})^{T}$:

$$-\kappa_j^2\begin{pmatrix}1&0\\0&1\end{pmatrix}\vec{\xi}_j-2\kappa_j\sqrt{k_0^2+K_0^2}\begin{pmatrix}1&0\\0&-1\end{pmatrix}\vec{\xi}_j+\begin{pmatrix}\Delta_+&\alpha K_+^2\\ \alpha K_-^2&\Delta_-\end{pmatrix}\vec{\xi}_j=0. \quad (11)$$

Here $\alpha=(1+\theta\tilde{g}-\theta)$, $\Delta_{\pm}=k_{\pm}^2-k_0^2+(1+\alpha)K_{\pm}^2-K_0^2$, $k_{\pm}^2=(\omega_0\pm\delta)^2[1+\hat{\chi}(\omega_0\pm\delta)]$, $K_{\pm}^2=(\omega_0\pm\delta)^2\overline{\chi^{(3)}}|E_0|^2/(c^2S_{mod})$, and $\tilde{g}(\delta)$ is the Fourier transform of the response function $g(t)$:

$$\tilde{g}(\delta)=\int_{-\infty}^{+\infty}g(t)\exp(-i\delta t)dt=\frac{\tau_1^2+\tau_2^2}{\tau_2^2+\tau_1^2(1+i\delta\tau_2)^2}. \quad (12)$$

κ_j are the roots of the fourth-order algebraic equation:

$$\kappa^4-[4(k_0^2+K_0^2)+\Delta_++\Delta_-]\kappa^2+2\sqrt{k_0^2+K_0^2}(\Delta_+-\Delta_-)\kappa+(\Delta_+\Delta_--\alpha^2K_+^2K_-^2)=0. \quad (13)$$

As far as we know, all previous results on FWM in fibers with nontrivial dispersion characteristics have relied on the slowly varying approximation in z and thereby resulted in a quadratic equation for κ, see, e.g., Refs. [1,12–14]. As we will discuss in more details in Sec. III, the two extra roots can describe excitation of both forward and backward waves. Equation (13) also fully accounts for the dispersion profile of the fiber and it is valid practically for arbitrary values of δ.

Solution (7) becomes unstable if Eq. (13) has at least one root with $\mathrm{Im}(\kappa)<0$. Knowing k as a function of ω and solving Eq. (13) numerically we can plot the dependencies of all four eigenvalues κ on any parameter. Since Eq. (13) requires a knowledge of the function $k(\omega)$, we start considering the example of a TF, for which this dependence is easy to calculate [11]. First, we fix the pump frequency ω_0 at $2\pi\times250$ THz, where the GVD is large and anomalous. Corresponding values of GVD and γ are $\beta_2\simeq-53$ ps^2/km and $\gamma=0.165$ W^{-1} m^{-1}. Figure 2 shows the δ dependence of the imaginary and real parts of all four roots of Eq. (13). Two roots, κ_2 and κ_4, have negative imaginary parts and generate instabilities.

Here and in what follows it is sufficient for us to plot only values of κ for $\delta>0$. From Eq. (10), it is clear that plots for $\delta>0$ give us full information about both the Stokes and the anti-Stokes waves. It is also obvious from Eq. (10) that any instability leads to the same growth rate for the Stokes and anti-Stokes waves having the same index j. What, however, makes the intensities of the two waves physically different is the ratio of the z-independent amplitudes:

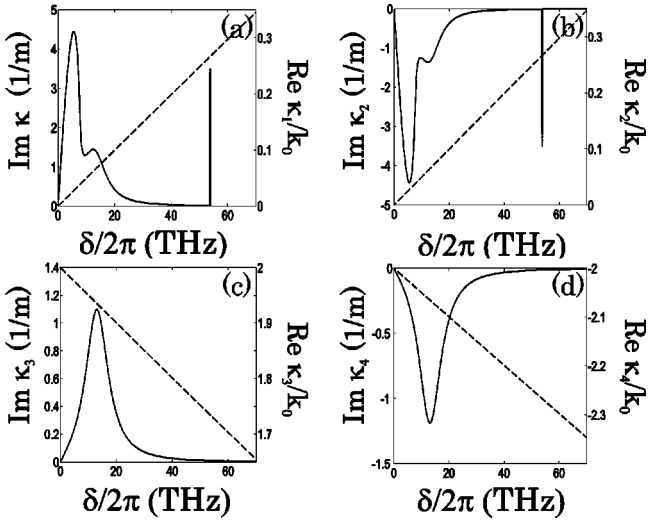

FIG. 2. Imaginary (solid lines, see scale on the left vertical axes) and normalized real (dashed lines, see scale on the right vertical axes) parts of the roots of Eq. (13). $k(\omega)$ is taken for the TF with $d=1$ μm, see Fig. 1(b) for the corresponding GVD profile. Pump frequency is $\omega_0/(2\pi)=250$ THz and pump power $E_0^2=200$ W.

$$R_j=\frac{|u_j^{AS}|}{|u_j^{S}|}, \quad j=1,2,3,4, \quad (14)$$

which can be calculated from our linear theory. Coefficients $R_{2,4}$, corresponding to the pair of unstable eigenvalues from Fig. 2, are shown in Fig. 3 as functions of the detuning δ (see Sec. III for more details).

The left-most instability band shown in Fig. 2(b) has a direct analog in the idealized NLS equation in the anomalous dispersion regime (see Sec. IV). The far-detuned instability peak, however, does not exist in the idealized NLS—it appears in our model due to modified fiber dispersion. This peak is always narrow compared to the primary one. Figure 4 shows dependence of the detuning and the maximal value of $\mathrm{Im}\,\kappa_2$ on the pump frequency.

Taking dispersion profiles for the TFs with progressively larger-core radii, i.e., approaching the limit of the conventional fibers, we have demonstrated that the secondary FWM peak moves towards the larger values of δ. Reference [14] is the only report known to us of the existence of similar sec-

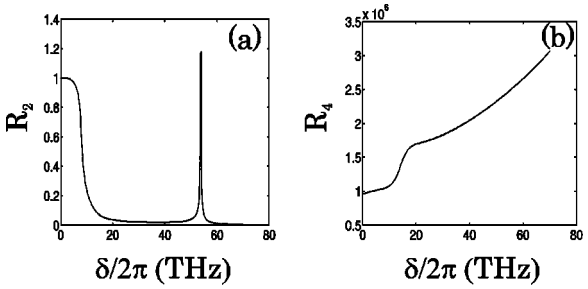

FIG. 3. δ dependence of the ratios of the amplitudes of Stokes and anti-Stokes waves, $R_{2,4}$, corresponding to the pair of unstable eigenvalues from Figs. 2(b) and 2(d). Values of parameters are the same as Fig. 2. Note the difference in the scale between (a) and (b).

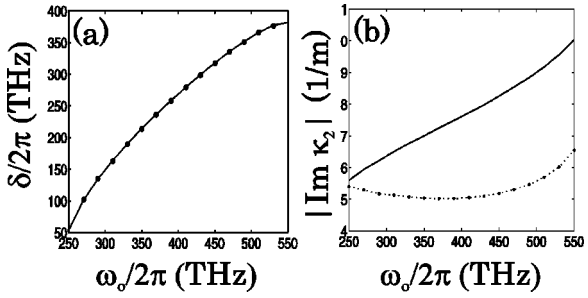

FIG. 4. (a) Dependence of the position of the maximum of the second FWM peak on the pump frequency. (b) Dependence of the gain at the maximum of the second FWM peak on the pump frequency. Full lines are obtained using wave equation, see Eq. (13), and dotted lines are obtained using generalized NLS equation, see Eq. (16). $k(\omega)$ is taken for the TF with $d=1$ μm, see Fig. 1(b) for the corresponding GVD profile, and pump power is $E_0^2=200$ W.

ondary peaks in fibers with flattened GVD. However, small-core PCFs and TFs have GVD profiles which, in some important aspects, are different from the parabolic approximation for $\beta_2(\omega)$ used in Ref. [14] (see Sec. IV for discussion of these differences).

If one neglects the Raman effect by putting $\theta=0$, then the imaginary parts of $\kappa_{3,4}$ are equal to zero and the instability associated with κ_4, disappears. An important feature of the instabilities induced by the Raman effect is that their existence does not depend on the sign of β_2. Indeed in Fig. 5 we show plots of imaginary parts of all four eigenvalues for a TF when the pump frequency is taken at $\omega_0/(2\pi)=600$ THz, i.e., deep inside the normal GVD regime. One can see that the gain maxima of the existing instability domains are at $\delta\simeq 13$ THz, which corresponds to the maximum of the Raman gain.

III. STOKES VS ANTI-STOKES AND FORWARD VS BACKWARD WAVES

Because the wave equation has a second-order derivative in z it naturally includes backward waves. One can see from

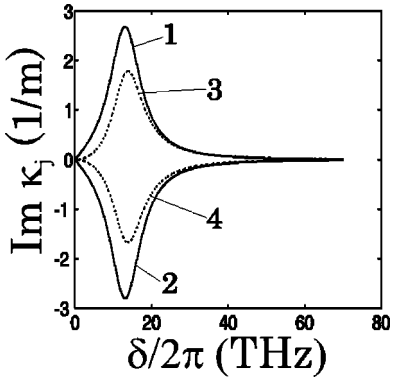

FIG. 5. δ dependence of the imaginary parts of the four roots of Eq. (13) in the deep normal dispersion regime. $k(\omega)$ is taken for the TF with $d=1$ μm, see Fig. 1(b) for the corresponding GVD profile. Pump frequency $\omega_0/(2\pi)=600$ THz and pump power $E_0^2=200$ W. Numbers correspond to the root index j in Eq. (13).

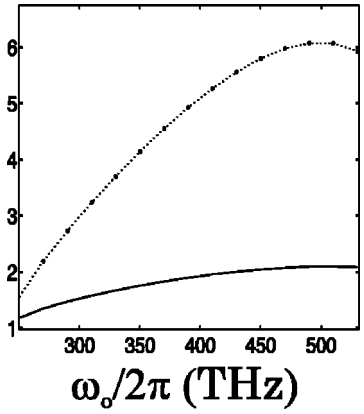

FIG. 6. Ratio of the amplitudes of Stokes and anti-Stokes waves corresponding to the second FWM peak as function of the pump frequency, for a pump power $E_0^2=200$ W. Full lines are obtained using wave equation, see Eq. (13), and dotted lines are obtained using generalized NLSE, Eq. (16).

Fig. 2 that $0<\mathrm{Re}\,\kappa_{1,2}/k_0<1$, which means, see Eqs. (10), that both Stokes and anti-Stokes waves excited by the unstable root κ_2 are forward waves, i.e., they copropagate with the pump wave. Contrary, looking at the Figs. 2(c,d), one can observe that Stokes and anti-Stokes waves corresponding to the root κ_4 are, respectively, backward and forward waves, $\mathrm{Re}\,\kappa_4/k_0<-2$. The situation is opposite for κ_3, $\mathrm{Re}\,\kappa_3/k_0<2$, but this root does not generate any unstable bands. Thus one can conclude that the Stokes wave excited by the unstable root κ_4 propagates backwards and the corresponding unstable anti-Stokes wave copropagates with the pump. Note that amplitude of the backward Stokes wave is predicted to be 10^6 times less than the amplitude of the forward anti-Stokes wave, see Fig. 3(b). What is important, however, that the strong forward anti-Stokes wave corresponding to κ_4 is completely disregarded in the standard slowly varying approximation, see Sec. IV, though its contribution to FWM process is of the same order of magnitude as the one associated with κ_2.

Analyzing dependence of R_2 on δ [Fig. 3(a)], one can see that the first FWM peak corresponds to a wave with a Stokes component slightly stronger than the anti-Stokes one. In contrast, the second peak generates a stronger anti-Stokes wave. We have found that this situation is typical for a wide range of pump frequencies and pump powers. The dependence of R_2 (corresponding to the maximum gain of the second FWM peak) on pump frequency is shown in Fig. 6.

IV. COMPARISON BETWEEN THE WAVE AND GENERALIZED NLS EQUATIONS

A. Theory of FWM in generalized NLS equation

Different variants of the generalized NLS equation have been so far the most popular approach to the theoretical and numerical analyses of nonlinear effects in fibers with complex dispersion, including PCFs, see, e.g., Refs. [9,10,14–16]. The rigorous analysis developed above allows evaluation of the validity of the generalized NLS equation and, as

we will demonstrate below, uncovers some significant discrepancies between the two approaches.

Assuming that $\overline{E}=(S_{mod})^{-1/2}A(z,\tau)e^{ik_0z-i\omega_0t}+\text{c.c.}$, $\tau=t-z\beta_1$, and using the procedure outlined in Ref. [17] we derive an equation describing evolution of the envelope function A:

$$i(\partial_z-i\hat{D})A=-\gamma\left[1+\frac{i}{\omega}\partial_\tau\right]A\left((1-\theta)|A|^2+\theta\int_{-\infty}^{+\infty}g(\tau-\tau')|A(z,\tau')|^2d\tau'\right),$$

$$\hat{D}(i\partial_t)\equiv\sum_{n=2}^{N}\frac{\beta_n}{n!}(i\partial_\tau)^n. \tag{15}$$

Here $\beta_n=\partial_\omega^n k$ are the dispersion coefficients calculated for $\omega=\omega_0$. The summation in $\hat{D}$ should be taken up to an order N high enough to ensure that the dispersion profile is adequately approximated in the frequency domain under consideration. In our calculations we used $N=20$. The τ derivative in the right-hand side of Eq. (15) describes self-steepening effects, i.e., the intensity dependence of the group velocity, see, e.g., Refs. [1,12,17].

FWM instabilities for different variations of Eq. (15) have been previously analyzed by many authors, see, e.g., Refs. [12–14]. For this reason we focus only on details important to this work, i.e., those that are relevant either in the PCF and TF context or in comparisons with the FWM analysis of the wave equation. We will also identify a condition for maximizing the FWM gain, which is not related to the well-known wave-vector-matching condition, but rather to the matching of group velocities.

The CW solution of Eq. (15) has the form $A=E_0\exp\{iK_0^2z/(2k_0)\}$ [see Eq. (8) for link between K_0 and $|E_0|^2$]. To study the stability of this solution we perturb it with a small signal in form (10) and derive the following quadratic equation for κ:

$$\kappa^2+(a_{11}+a_{22})\kappa+a_{11}a_{22}-a_{12}a_{21}=0, \tag{16}$$

where

$$a_{11}=-\hat{D}(-\delta)+K_0^2[1-(1+\alpha)(1-\delta/\omega_0)]/(2k_0),$$

$$a_{12}=-\alpha K_0^2(1-\delta/\omega_0)/(2k_0),$$

$$a_{21}=\alpha K_0^2(1+\delta/\omega_0)/(2k_0),$$

$$a_{22}=\hat{D}(\delta)-K_0^2[1-(1+\alpha)(1+\delta/\omega_0)]/(2k_0).$$

For clarity of interpretation of the instability peaks shown in Fig. 2(b), let us assume that $\theta=0$ and neglect self-steepening effects. After some algebra, the instability growth rate can be presented in the form

$$2\,\text{Im}\,\kappa_2=-\,\text{Im}\sqrt{[\hat{D}(\delta)+\hat{D}(-\delta)][\hat{D}(\delta)+\hat{D}(-\delta)+K_0^2/k_0]}, \tag{17}$$

where the imaginary part of the square root is fixed to be positive and $\kappa_{1,2}$ are the two roots of Eq. (16).

B. Interpretation of the FWM instabilities

Substituting any of the roots of Eq. (16) into Eq. (10) and calculating the overall wave vectors of the Stokes, $k_S=k_0+K_0^2/(2k_0)-\text{Re}\,\kappa$, and anti-Stokes, $k_{AS}=k_0+K_0^2/(2k_0)+\text{Re}\,\kappa$, waves one can see that the phase-matching condition for these waves is satisfied automatically under all conditions: $2[k_0+K_0^2/(2k_0)]\equiv k_S+k_{AS}$. The condition for the onset of FWM instabilities is that $\text{Re}\,\kappa_1=\text{Re}\,\kappa_2$, which is satisfied throughout the entire instability domain, but not outside it. Thus the emergence of FWM instabilities implies the existence of phase synchronism between the two eigenperturbations in Eq. (10).

The previously introduced parameters k_+ and k_- correspond to the wave vectors of two independent, i.e., not linked by Eqs. (10) and (11), waves. Obviously, there are good grounds to call them Stokes $(-)$ and anti-Stokes $(+)$ waves, but this should be done with a degree of caution. This is because it is easy to confuse them with the previously introduced Stokes and anti-Stokes waves, which have completely different dispersive characteristics determined by Eq. (13) or (16). One can note that $\hat{D}(\delta)+\hat{D}(-\delta)=k_++k_--2k_0\equiv\Delta k_l$, where Δk_l is the linear mismatch between the wave vectors. Taking into account that the generation of Stokes and anti-Stokes photons requires two pump photons, one can easily show that the mismatch between the nonlinear parts of the wave vectors is given by $\Delta k_{nl}=K_0^2/k_0$ (note that in our notations Δk_{nl} is always positive). One can see that condition for the FWM instabilities $\text{Re}\,\kappa_1=\text{Re}\,\kappa_2$ is satisfied providing

$$-\Delta k_{nl}<\Delta k_l<0, \tag{18}$$

i.e., Δk_l is always negative within the instability domain. It is clear now that FWM instability starts either when the matching for the full (linear+nonlinear) wave vectors is satisfied, i.e., when $\Delta k_l+\Delta k_{nl}=0$, or when only the linear parts of the wave vectors are matched, i.e., when $\Delta k_l=0$.

Figure 7 shows regions of FWM instability in the $(\delta,|E_0|^2)$ plane calculated using Eq. (13). Use of Eq. (16) leads to almost the same results. In Fig. 7(a) one can see that as pump power is increasing, both FWM bands become broader until, at some critical power, they merge into a single band. The critical power for this merging is probably too high to have practical relevance in the cw regime. For powers even higher, there exists a second threshold when all instabilities disappear [see Fig. 7(b)]. This effect exists also in the absence of the second FWM peak and becomes possible due to self-steepening. It is therefore not described by the simplified Eq. (17); however, it can be predicted by Eq. (16). Suppression of the instability due to self-steepening

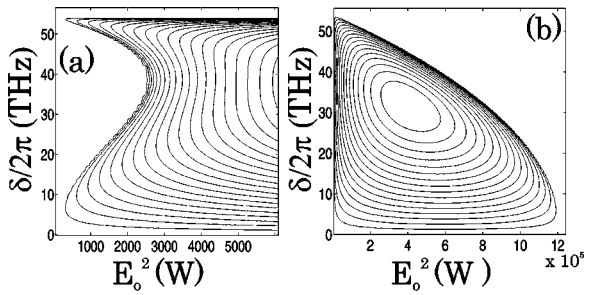

FIG. 7. Level plots of $\mathrm{Im}\kappa_2$ showing regions of FWM instabilities in the (δ, E_0^2) plane calculated using Eq. (13), for two different ranges of power, using a pump frequency of $\omega_0/2\pi = 250$ THz. (a) clearly shows the independence of the secondary FWM peak from power and the existence of a critical power at which the two peaks merge, while (b) shows the existence of a second critical power where all the instabilities disappear.

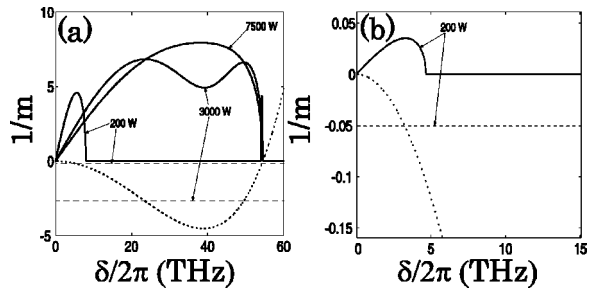

FIG. 8. (a) Full lines correspond to $|\mathrm{Im}\,\kappa_2|$ calculated for the TF example using Eq. (17). Pump power is indicated explicitly and the other parameters are the same as for Fig. 2(b). $\Delta k_l(\delta)$ is plotted by the doted line. Dashed horizontal lines indicate $-\Delta k_{nl}/2$ for different powers. Intersections of the dashed and dotted lines correspond to the positions of the maxima of the FWM gain before merging. After the merging, maximum of the gain corresponds to the minimum of Δk_l. (b) Same as (a), but for the conventional (SMF28) fiber, see Fig. 1, pumped at $\omega_0/(2\pi) = 250$ THz. Note that to make (a) and (b) readable we had to scale the plotted values. $\mathrm{Im}\,\kappa_2$ corresponding to 3 kW and 7.5 kW were divided, respectively, by 10 and 20. $\Delta k_{l,nl}$ were divided by the factor 200.

was previously described by Potasek [12] for another variant of the generalized NLS equation.

The gain maxima in the first and second instability bands [see Figs. 2(b) and 7(a) for $E_0^2 < 2500$ W] correspond to zeros of the derivative of Eq. (17) with respect to δ, and can be found from the condition

$$\Delta k_l + \tfrac{1}{2}\Delta k_{nl} = 0. \tag{19}$$

This condition shows that, for maximum gain, the linear wave-vector mismatch Δk_l must be compensated by half the nonlinear mismatch. It is important to note, that if Δk_l is negative for all δ and $\partial_\delta \Delta k_l$ is also always negative, then, for a given power, condition (19) can be satisfied for one particular value of $|\delta|$ only. If, however, $\partial_\delta \Delta k_l$ changes its sign several times for $\delta > 0$, then there is always a range of pump powers where condition (19) is satisfied at least twice. For the PCF and TF, one can show that $\partial_\delta \Delta k_l$ changes its sign once, which ensures the existence of a secondary FWM peak [see Fig. 8(a)]. The dispersion of a conventional fiber, see Fig. 1, however, gives a monotonic decay of Δk_l with δ [Fig. 8(b)] and therefore only a single FWM peak exists in this case.

From Fig. 8(a) it is clear that condition (19) cannot be satisfied if the pump power is high enough to make $\Delta k_{nl} > 2|\min_\delta \Delta k_l|$. It is also clear that on approaching this threshold, the two FWM bands merge into one [see Figs. 7(a) and 8(a)]. However, the instability still exists when $\Delta k_{nl} > 2|\min_\delta \Delta k_l|$. Now, the position of the maximum of the FWM gain is given by a second condition ensuring that the derivative of Eq. (17) with respect to δ is zero, which, as can be easily shown, is

$$\frac{\partial \Delta k_l}{\partial \delta} = 0. \tag{20}$$

Figure 8(a) illustrates that the minimum of the curve Δk_l exactly corresponds to the maximum of the gain after the merging of two FWM bands. k_0 is obviously does not depend on δ and therefore condition (20) transforms into

$$\beta_1|_{\omega=\omega_0+\delta} - \beta_1|_{\omega=\omega_0-\delta} = 0. \tag{21}$$

Thus the maximum of the gain now happens for values of δ where the *Stokes and anti-Stokes waves have the same group velocities*.

C. Discrepancies between the wave and generalized NLS equations

Any discrepancies between the predictions of Eqs. (13) and (16) for $\mathrm{Im}\,\kappa_2$ and R_2, at values of detuning corresponding to the first FWM peak, are negligible for all relevant parameters. We therefore concentrate our attention on the second FWM peak. Let us first point out that the large values of detuning for the second FWM peak can either violate or endanger one of the main assumptions used to derive the generalized NLS equation, namely, $|\delta|/\omega \ll 1$. Plotting the position of the second, i.e., far-detuned, FWM peak as a function of the pump frequency [see Fig. 4(a)], we find that the results obtained from Eqs. (13) and (16) are very close. This is because the position of the secondary FWM is primarily determined by the GVD profile of the system, which is taken into account by Eq. (15) almost exactly. However, the gain and relative strength of the Stokes and anti-Stokes components for this peak strongly depend on the dispersion of the nonlinearity. Because the dependence of the nonlinearity on δ is taken into account by Eq. (15) only approximately, substantial discrepancies occur between the predictions of Eqs. (5) and (15) for values of $\mathrm{Im}\,\kappa_2$ and R_2, see Figs. 4(b) and 6. Thus Eq. (15) is often insufficient for quantitative comparisons between experimental and theoretical results. Let us mention again that Eq. (15) also completely fails to take into account excitation of the strong forward anti-Stokes and weak backward Stokes waves associated with the unstable root κ_4, see Fig. 2(d).

D. Role of higher-order dispersion

Figure 9 shows regions of FWM instability in the (δ, ω_0) plane, calculated using Eq. (13). Use of Eq. (16) again leads

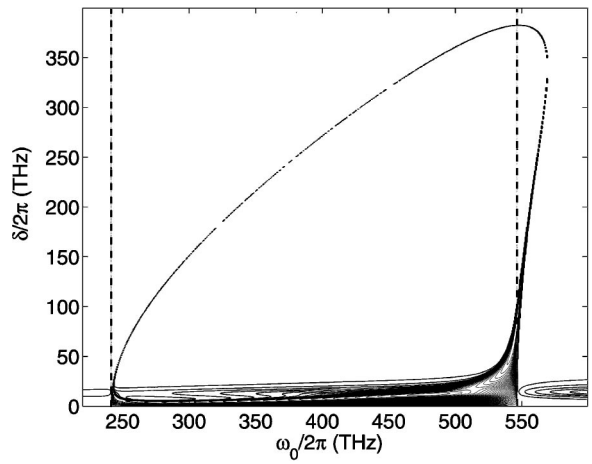

FIG. 9. Level plots of Im κ_2 showing regions of FWM instabilities in the (δ,ω_0) plane, calculated using Eq. (13), for a pump power of $P=200$ W. The two dashed vertical lines mark the zero GVD points. The unstable regions existing for normal GVD and centered approximately at 13 THz correspond to the Raman gain. In the proximity of the high-frequency zero GVD point there is a region of frequencies in which the far-detuned FWM peaks, not related to the Raman effect, exist even when the fiber is pumped in the normal GVD region.

to very similar results. It is clear that the position of the second FWM peak is very sensitive to changes in the pump frequency. For example, this peak is located much closer to the pump frequency near to the left-most, i.e., low-frequency, zero GVD point. Looking at Figs. 1 and 10 one can see that the curvature of the $\beta_2(\omega)$ plot, i.e., β_4, is positive on the right from the low-frequency zero GVD point, and negative on the left from the high-frequency zero GVD point, with the sign change happening around $\omega/(2\pi)\simeq 370$ THz. Neglecting powers of δ higher than four in the expressions for $\hat{D}$ $(\pm\delta)$, one can see that, if both β_2 and β_4 are negative, then $\Delta k_l \simeq \beta_2\delta^2+\frac{1}{12}\beta_4\delta^4$ and $\partial_\delta \Delta k_l$ are always negative. Therefore, condition (19) can be satisfied only once, which gives the first FWM peak. A change in the sign of $\partial_\delta \Delta k_l$ and the existence of the second FWM peak are ensured only by positive $(n\geqslant 6)$ higher-order dispersion terms. This, however, requires sufficiently large values of δ, because higher-order dispersions are very small. See Fig. 10 for comparison of β_2, β_4, and β_6.

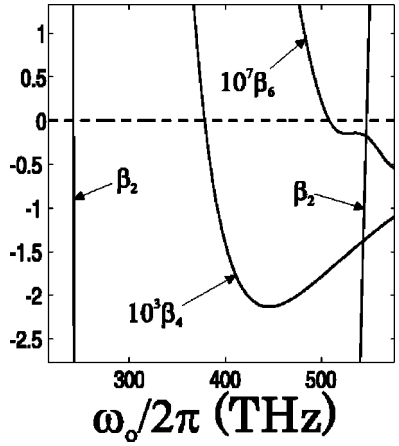

FIG. 10. Plots of $\beta_{2,4,6}$ vs ω for 1-μm tapered fiber. $\beta_{2,4,6}$ are measured, respectively, in ps^2/km, ps^4/km, ps^6/km.

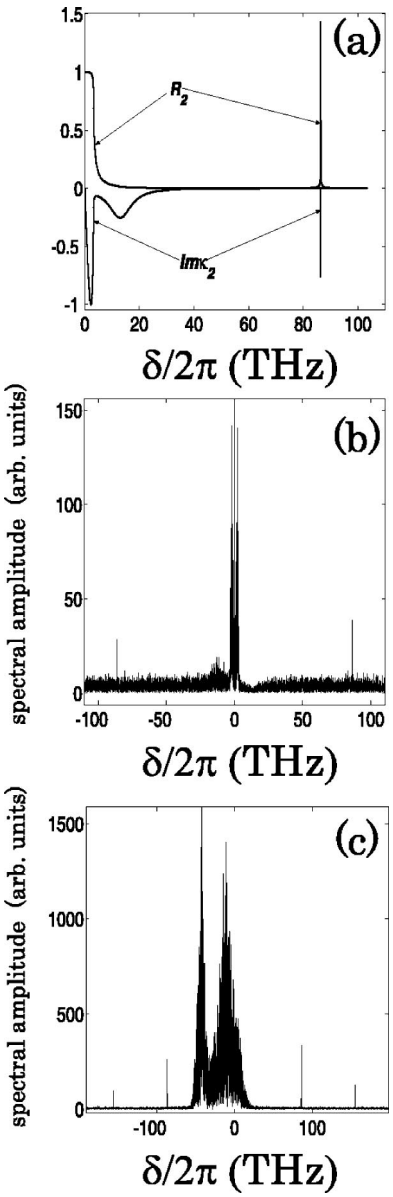

FIG. 11. (a) Im κ_2, characterizing FWM gain, and R_2, characterizing ratio of the intensities of the Stokes and anti-Stokes components. Dispersion profile was taken as for PCF shown in Fig. 1(b), with $\omega_0/(2\pi)=250$ THz and $|E_0|^2=43$ W. (b) Results of the numerical modeling of Eq. (15). Parameters are the same as for (a) and propagation distance is 0.5 m. (c) Same as (b), but with $|E_0|^2=200$ W.

For these reasons, use of the parabolic approximation for the GVD profile [i.e., fixing ω_0 at the β_2 minimum and using only β_2 and β_4 in the expansion for $\hat{D}(\delta)$] will fail to predict correctly the position of the second FWM peak in our fibers. The theory developed in Ref. [14], in a different context but also predicting a second FWM peak, uses the parabolic approximation for the GVD and therefore cannot be directly applied to PCFs and TFs. Let us point out that the

importance of higher-order dispersion also manifests itself in the fact that FWM gain exists in the finite region of normal GVD adjacent to the high-frequency zero GVD point—see Fig. 9. It is important to note that this gain region is insensitive to the presence or absence of the Raman gain, which generates an instability peaking at $\delta \simeq 13$ THz for any ω_0.

E. Numerical modeling of the generalized NLS equation

All the above results, for the dispersion profile of a 1 μm tapered fiber, can be used to characterize the FWM instabilities for a PCF with dispersion profile shown in Fig. 1. Figure 11(a) shows $\mathrm{Im}\kappa_2$ and R_2 calculated using Eqs. (15) and (16) and corresponding to a PCF pumped at $\omega_0/(2\pi) = 250$ THz. Comparing this plot with Figs. 2(b) and 3(a) for a TF, the main difference is that the detuning of the second FWM is larger in the PCF, which is due merely to the fact that the ratio of the corresponding $|\beta_4|$ and $|\beta_2|$ is smaller at this pump frequency. Results of numerical modeling of Eq. (15), showing the spectrum of the radiation after 0.5 m of propagation at pump power $E_0^2 = 43$ W, can be seen in Fig. 11(b). This is in full agreement with analytical predictions of the positions of the FWM peaks and the relative strengths of the Stokes and anti-Stokes components [compare Figs. 11(a) and (b)]. For higher powers the spectrum of the primary FWM bands broadens and is Raman shifted towards lower frequencies. Secondary FWM peaks can still be clearly observed, together with second-order side bands [see Fig. 11(c)].

V. SUMMARY

We have developed a theory of FWM in ultrasmall core optical fibers with overall dispersion profiles strongly modified by waveguide dispersion, using tapered and photonic-crystal fibers as examples. Our approach avoids use of the traditional slowly varying approximation and relies on analysis of the full wave equation. We have predicted the existence of a secondary FWM peak that does not exist in conventional fibers and large-core PCFs, and studied its properties in detail. Existence of this peak and strong dependence of its detuning on the pump frequency, together with the reduced power requirements for the small-core fibers, can potentially lead to the design of new kinds of parametric amplifiers and oscillators. Let us stress that detuning of the secondary FWM peaks from the pump wave tends to infinity together with the low-frequency zero GVD point shifting to the far ''red'' part of the spectrum, when the core diameter of the TF or equivalent PCF is increased. This is the primary reason why the secondary FWM peak has not been reported in the previously published literature on PCFs, where the low-frequency zero GVD point and the entire part of the dispersion characteristic with negative slope of $\beta_2(\omega)$ were not present in the practically relevant part of the spectrum, see, e.g., Refs. [7–10].

Comparison of the results obtained from the wave equation with the corresponding results derived from the generalized NLS equation reveals a number of deficiencies in the latter. In particular, the NLS fails to predict correctly the gain and relative strength of the Stokes and anti-Stokes components associated with the secondary FWM peak. It also completely disregards the existence of a pair of additional forward anti-Stokes and backward Stokes waves excited by the Raman effect.

We have also shown that under certain conditions position of the maximum of FWM gain can be determined not simply by the wave-vector matching, but by the equality of the group velocities of the Stokes and anti-Stokes waves.

ACKNOWLEDGMENTS

We are grateful to Feng Luan for providing us with experimental measurements of the PCF dispersion profile. We acknowledge useful discussion with Tim Birks, Jonathan Knight, and A. Ortigosa-Blanch. This work was partially supported by the Royal Society.

[1] G.P. Agrawal, *Nonlinear Fiber Optics* (Academic Press, San Diego, 2001).
[2] J.C. Knight, T.A. Birks, J.C. Knights, and P.St.J. Russell, Opt. Lett. **21**, 1547 (1996).
[3] P.St.J. Russell, Science **299**, 358 (2003), and references therein.
[4] B.J. Eggleton, C. Kerbage, P. Westbrook, R.S. Windeler, and A. Hale, Opt. Express **9**, 698 (2001), and references therein.
[5] J.H. Lee, Z. Yusoff, W. Belardi, M. Ibsen, T.M. Monro, and D.J. Richardson, Opt. Lett. **27**, 927 (2002).
[6] T.A. Birks, W.J. Wadsworth, and P.St.J. Russell, Opt. Lett. **25**, 1415 (2000).
[7] J.E. Sharping, M. Fiorentino, A. Coker, P. Kumar, and R.S. Windeler, Opt. Lett. **26**, 1048 (2001).
[8] G. Millot, A. Sauter, J.M. Dudley, L. Provino, and R.S. Windeler, Opt. Lett. **27**, 695 (2002).
[9] S. Coen, A.H.L. Chau, R. Leonhardt, J.D. Harvey, J.C. Knight, W.J. Wadsworth, and P.St.J. Russell, J. Opt. Soc. Am. B **19**, 753 (2002).
[10] J.M. Dudley, L. Provino, N. Grossard, H. Maillotte, R.S. Windeler, B.J. Eggleton, and S. Coen, J. Opt. Soc. Am. B **19**, 765 (2002).
[11] A.W. Snyder and J.D. Love, *Optical Waveguide Theory* (Chapman and Hall, London, 1983).
[12] M.J. Potasek, Opt. Lett. **12**, 921 (1987).
[13] K.J. Blow and D. Wood, IEEE J. Quantum Electron. **25**, 2665 (1989).
[14] M. Yu, C.J. McKinstrie, and G.P. Agrawal, Phys. Rev. E **52**, 1072 (1995).
[15] J. Herrmann, U. Griebner, N. Zhavoronkov, A. Husakou, D. Nickel, J.C. Knight, W.J. Wadsworth, P.St.J. Russell, and G. Korn, Phys. Rev. Lett. **88**, 173901 (2002).
[16] A.L. Gaeta, Opt. Lett. **27**, 924 (2002).
[17] T. Brabec and F. Krausz, Phys. Rev. Lett. **78**, 3282 (1997).